

# Prospects for differentiating extended coronal geometries in AGNs with the *IXPE* mission

F. Ursini,<sup>1</sup>★ G. Matt,<sup>1</sup> S. Bianchi,<sup>1</sup> A. Marinucci,<sup>2</sup> M. Dovčiak,<sup>3</sup> and W. Zhang<sup>4</sup>

<sup>1</sup> *Dipartimento di Matematica e Fisica, Università degli Studi Roma Tre, via della Vasca Navale 84, 00146 Roma, Italy*

<sup>2</sup> *ASI - Italian Space Agency, Via del Politecnico snc, 00133, Rome, Italy*

<sup>3</sup> *Astronomical Institute, Academy of Sciences of the Czech Republic, Boční II 1401, CZ-14100 Prague, Czech Republic*

<sup>4</sup> *National Astronomical Observatories, Chinese Academy of Sciences, 20A Datun Road, Beijing 100101, China*

Accepted XXX. Received YYY; in original form ZZZ

## ABSTRACT

X-ray polarimetry can potentially constrain the unknown geometrical shape of AGN coronae. We present simulations of the X-ray polarization signal expected from AGN coronae, assuming three different geometries, namely slab, spherical and conical. We use the fully relativistic Monte-Carlo Comptonization code `MONK` to compute the X-ray polarization degree and angle. We explore different coronal parameters such as shape, size, location and optical depth. Different coronal geometries give a significantly different X-ray polarization signal. A slab corona yields a high polarization degree, up to 14% depending on the viewing inclination; a spherical corona yields low values, about 1–3%, while a conical corona yields intermediate values. We also find a difference of 90 degrees in polarization angle between the slab corona and the spherical or conical coronae. Upcoming X-ray polarimetry missions like *IXPE* will allow us to observationally distinguish among different coronal geometries in AGNs for the first time.

**Key words:** black hole physics – galaxies:active – galaxies:Seyfert – X-rays:galaxies – polarization

## 1 INTRODUCTION

An X-ray corona is one of the main constituents of active galactic nuclei (AGNs) and primary contributor to their X-ray emission (e.g. Haardt & Maraschi 1991). The corona is situated in the innermost region of the accretion flow and in the close proximity to the event horizon of the central supermassive black hole (Reis & Miller 2013, e.g.). Indeed, microlensing studies show that the size of the X-ray corona is of the order of a few gravitational radii (e.g. Chartas et al. 2009, 2016). The X-ray emission of AGNs thus provides a powerful probe of General Relativity in the strong gravity regime. However, the physical origin of the corona is a matter of debate, although magnetic processes are often invoked for its formation and heating (e.g. Di Matteo 1998). The origin of the corona is related to its geometry, which is essentially unknown. The corona could be a sphere-like region above the black hole, possibly powered by magnetic reconnection (e.g. Wilkins & Fabian 2012), or it could have a conical shape if it forms the base of a jet (e.g. Henri & Pelletier 1991; Henri & Petrucci 1997; Markoff et al. 2005) or a failed jet (Ghisellini et al. 2004). The corona could also be a slab-like structure sandwiching the accretion disc (e.g. Haardt & Maraschi 1993), perhaps originating from magnetic instabilities (e.g. Di Matteo 1998). Constraining the coronal geometry is thus of prime importance to shed light on the physics of the disc-corona system.

Currently, constraints on the coronal geometry can only be derived from spectral and/or timing properties, such as the analysis of time lags between different energy bands (e.g. De Marco et al. 2013; Kara

et al. 2016; Caballero-García et al. 2020). In principle, polarimetry could yield more direct and model-independent measurements. Indeed, the polarization properties of the radiation crucially depend on the geometry of the emitting system. In AGNs, the primary emission from the corona could be significantly polarized (e.g. Haardt & Matt 1993; Poutanen & Vilhu 1993; Schnittman & Krolik 2010; Dovčiak et al. 2011; Tamborra et al. 2018). The polarization of X-rays reprocessed by the disc and surrounding material can be a powerful probe of the disc/corona geometry (e.g. Matt et al. 1989, 1993), especially in Seyfert 2 galaxies, in which relatively high polarization degrees are expected (Marin et al. 2018a). Seyfert 1 galaxies, on the other hand, offer a more direct view of the corona: their 2–10 keV emission is usually dominated by the primary power law, and its polarimetric properties can be used to constrain the geometrical shape of corona (e.g. Beheshtipour et al. 2017).

X-ray polarimetric studies of AGNs will become possible for the first time thanks to the Imaging X-ray Polarimetry Explorer (*IXPE*, Weisskopf et al. 2016), a NASA/ASI mission that has been successfully launched on December 9, 2021. *IXPE* is the first X-ray mission dedicated to polarimetry, carrying three X-ray telescopes with polarization-sensitive imaging detectors (the gas-pixel detectors, Costa et al. 2001) operative in the 2–8 keV band (Weisskopf et al. 2016). *IXPE* is expected to perform meaningful measurements of the X-ray polarization of different types of sources, including AGNs (Weisskopf et al. 2016; Marin & Weisskopf 2017). An X-ray polarimetry array will also be a key element of the enhanced X-ray Timing and Polarimetry mission (eXTP, Zhang et al. 2016), which is planned for launch in 2027.

In this work, we present numerical simulations of the X-ray polari-

★ E-mail: francesco.ursini@uniroma3.it

metric signal expected from the corona of radio-quiet, unobscured type 1 AGNs, using the general relativistic Monte Carlo radiative transfer code `MONK` (Zhang et al. 2019; Zhang et al., submitted). An analogous approach has been followed by Beheshtipour et al. (2017), who simulated the broad-band X-ray polarization signal of Seyfert 1 galaxies, for two corona geometries (wedge and spherical shell) and three different corona sizes. Our aim is to determine whether different coronal geometries can be distinguished with the polarimetric analysis of the primary X-ray emission, with an emphasis on upcoming *IXPE* observations. The paper is structured as follows. We discuss the application of the `MONK` code and the numerical setup in Sect. 2. We present the results in Sect. 3 and summarize our conclusions in Sect. 4.

## 2 SETUP

`MONK` calculates the energy and polarization spectra of Comptonized radiation from a corona illuminated by a standard accretion disc (Novikov & Thorne 1973). Here we briefly summarize the procedure implemented in `MONK`, referring to Zhang et al. (2019) for a detailed description. First, optical-UV seed photons are generated according to the disc emissivity, with initial polarization given by the calculation of Chandrasekhar (1960) for a semi-infinite planar atmosphere. Then, the photons are ray-traced along null geodesics in Kerr spacetime, propagating the polarization vector. Photons reaching the corona are Compton scattered assuming the Klein-Nishina cross section. The Stokes parameters of the scattered photons are computed in the electron rest frame (Connors et al. 1980) and then transformed in the observer (Boyer-Lindquist) frame. The propagation terminates when the photons either enter the event horizon, hit the disc or arrive at infinity. Counting the latter photons, the energy and polarization spectrum is constructed. Since scattering produces linearly polarized photons, the code computes the Stokes parameters  $Q$  and  $U$ , while  $V$  is set at zero.

The main input parameters of `MONK` are: the black hole mass and spin; the accretion rate; the physical (optical depth and temperature) and geometrical parameters of the corona. In our simulations, we set a black hole mass of  $2 \times 10^7$  solar masses and an Eddington ratio of 0.1. These parameters are chosen to be consistent with MCG-5-23-16, an AGN optically classified as a Seyfert 1.9 (Veron et al. 1980) with broad emission lines in the infrared (Véron-Cetty & Véron 2010; Onori et al. 2017a), likely viewed at an inclination of  $\sim 50$  deg (e.g. Zoghbi et al. 2017). This source is an excellent target for *IXPE*, being X-ray bright and Compton-thin (Baloković et al. 2015; Zoghbi et al. 2017). Its black hole mass is estimated from the X-ray variability (Ponti et al. 2012) and is consistent with the virial mass estimated from the infrared lines (Onori et al. 2017b). The Eddington ratio is set to 0.1 in agreement with the observed luminosity (Zoghbi et al. 2017). Concerning the black hole spin  $a$ , we make simulations assuming the two possible values  $a = 0$  and 0.998.

Different coronal geometries can be assumed in `MONK` (Zhang et al. 2019). Here we focus on three alternative configurations, namely the slab, the spherical lamppost, and the truncated cone, as we describe in the next sections (Fig. 1). Concerning the physical parameters of the corona, Baloković et al. (2015) reported measurements of the coronal optical depth  $\tau$  and temperature  $kT_e$  based on *NuSTAR* data of MCG-5-23-16. Zoghbi et al. (2017) also reported photon indices of 1.8–1.9 from the analysis of *Suzaku* and *NuSTAR* data of MCG-5-23-16 spanning 10 years. The *NuSTAR* spectra exhibit a well constrained high-energy cut-off between 100 and 200 keV (Baloković et al. 2015; Zoghbi et al. 2017). However, to obtain more

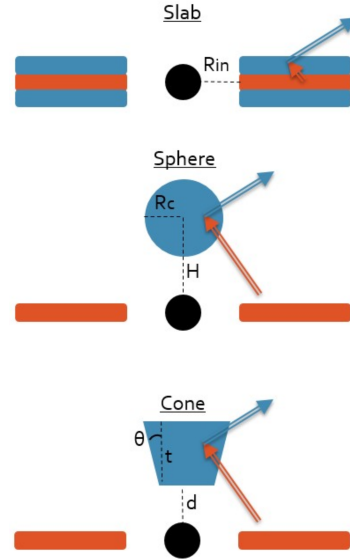


**Figure 1.** Different coronal geometries. The X-ray emission from the corona (in light blue) is produced by inverse Compton scattering of the optical-UV radiation from the disc (in orange).

general results and explore the relation between the polarimetric properties and the spectral shape, we proceed as follows. We assume three possible values of the photon index  $\Gamma$  of the primary power law in the 2–8 keV band, namely 1.6, 1.8, and 2. Then, for each value of  $\Gamma$ , we set three pairs  $\tau, kT_e$  consistent with it. In other words, we set  $\tau, kT_e$  such that the Comptonization spectrum produced by `MONK` is (a posteriori) consistent with a power law having the chosen photon index.

### 2.1 Slab

The slab corona is assumed to fully cover the disc, that can either be extended down to the innermost stable circular orbit (ISCO) or truncated at an arbitrary radius. In general, the ISCO depends on the black hole spin (e.g. Misner et al. 1973). We assume three possible values of the inner disc radius  $R_{in}$  (see also Table 1): (i)  $a = 0.998$ ,  $R_{in} = ISCO \equiv 1.24$  in units of gravitational radii ( $R_G = GM/c^2$ ); (ii)  $a = 0$ ,  $R_{in} = ISCO \equiv 6 R_G$ ; (iii)  $a = 0$ ,  $R_{in} = 30 R_G$  (truncated case). The vertical thickness of the slab corona is also a parameter of `MONK`, and we set it to  $1 R_G$  in all cases (see also Zhang et al. 2019). However, the results are not strongly dependent on this parameter. The physical parameters are summarized in Table 2: we set  $kT_e = 25, 50$  or  $100$  keV and an optical depth  $\tau$  consistent with the assumed photon index. In `MONK`, the optical depth in slab geometry is defined as  $\tau = n_e \sigma_T h$  where  $h$  is the half-thickness of the slab<sup>1</sup> (Zhang et al. 2019). The values of  $\tau$  in our simulations range between 0.25 and 1.65 (see Table 2). In the slab case, we assume the corona to be co-rotating with the Keplerian disc (Zhang et al. 2019).

<sup>1</sup> This definition is the same as in the popular Comptonization codes `COMPTT` (Titarchuk 1994) and `COMPPS` with `cov_frac`  $\neq 1$  (Poutanen & Svensson 1996).

**Table 1.** Geometrical parameters of the corona in the `MONK` simulations (in units of  $R_G$ ) for different values of the black hole spin  $a$ .

$a$	slab	sphere		cone	
	$R_{\text{in}}$	$H$	$R_c$	$d$	$t$
0.998	1.24	5	2	3	10
0	6	10	7	5	15
0	30	30	10	20	20

## 2.2 Spherical lamppost

A spherical lamppost corona is characterized by the height  $H$  above the disc and the coronal radius  $R_c$ . For the `MONK` simulations, we choose a few values of these two parameters following the estimates of the corona size by Ursini et al. (2020), obtained using the relativistic ray-tracing code of Dovčiak & Done (2016). These estimates are based on a simple argument: the corona must intercept a photon flux from the disc that is consistent with the observed X-ray flux, because Comptonization conserves the number of photons. The estimates of the lamppost corona size depend also on the spin; indeed, a larger spin allows for more compact corona closer to the event horizon (Ursini et al. 2020). We choose the following values of the coronal height and radius (see also Table 1): (i)  $a = 0.998$ ,  $H = 5 R_G$ ,  $R_c = 2 R_G$ ; (ii)  $a = 0$ ,  $H = 10 R_G$ ,  $R_c = 7 R_G$ ; (iii)  $a = 0$ ,  $H = 30 R_G$ ,  $R_c = 10 R_G$ . The optical depth in spherical geometry is the radial one, and its values in our simulations range between 0.8 and 4.5 (see Table 2). Finally, in the spherical case we assume a stationary corona (Zhang et al. 2019).

## 2.3 Truncated cone

If the corona is outflowing rather than static, for example forming the base of a jet, it might be better described as a conical blob opening away from the black hole. Since we focus on radio-quiet (i.e. non-jetted) Seyferts, following Ghisellini et al. (2004) we assume that the corona is a failed jet with a sub-relativistic bulk velocity, smaller than the escape velocity. In the scenario proposed by Ghisellini et al. (2004), blobs of material are launched with some initial velocity and then fall back, actually failing to produce a jet akin to that of radio-loud AGNs. In `MONK`, this type of corona is schematized as a single blob with a truncated conical shape, located on the symmetry axis of the disc, formed by electrons with a bulk velocity  $\beta$  (see Fig. 1, bottom panel). For consistency with the failed jet scenario, in our simulations we assume  $\beta = 0.3$ , which is less than the escape velocity at initial radii of 20-30  $R_G$  (Ghisellini et al. 2004). The three relevant geometrical parameters are the distance  $d$  between the lower base and the disc, the intrinsic height or thickness  $t$  of the truncated cone, and its half-opening angle  $\theta$ . The vertex of the cone is at the center of the black hole, so that the radius of the lower base is  $d \tan \theta$ . The optical depth in `MONK` is proportional to the diameter of the lower base, being defined as  $\tau = n_e \sigma_T 2d \tan \theta$ . Concerning the half-opening angle, we assume  $\theta = 30$  deg. The results are not much altered using different parameters, such as  $\beta = 0.1$  or  $\theta = 60$  deg, as long as  $\beta$  is not too close to unity.

## 3 RESULTS

We run 81 simulations with the parameters described above. To compute the polarization properties, for each simulation we assume an observer at different inclination angles, between 0 and 90 degrees (for a discussion of the dependency of the spectrum on the inclination,

**Table 2.** Physical parameters of the corona. The optical depth for the slab is vertical and measured from the half-plane of the disc, while it is radial for the spherical lamppost, and it depends on the diameter of the upper base for the truncated cone. The coronal temperature  $kT_e$  is in keV.

$\Gamma$	slab		sphere		cone	
	$\tau$	$kT_e$	$\tau$	$kT_e$	$\tau$	$kT_e$
1.6	0.55	100	1.5	100	1	100
	1	50	2.7	50	2	50
	1.65	25	4.5	25	3.2	25
1.8	0.35	100	1	100	0.7	100
	0.75	50	2	50	1.3	50
	1.35	25	3.5	25	2.3	25
2	0.25	100	0.8	100	0.5	100
	0.6	50	1.6	50	1	50
	1.15	25	3	25	1.7	25

see Zhang et al. 2019). We integrate the signal in the *IXPE* bandpass, namely 2–8 keV.

In the following sections, we plot the polarization degree and angle as a function of the cosine of the inclination angle  $\mu$ . The polarization angle is measured from the north-south direction in the sky plane, meaning that a polarization vector parallel to the disc corresponds to a polarization angle of 90 degrees. Below we focus on those coronal parameters that are in better agreement with the X-ray properties of MCG-5-23-16. We present in the appendix A the complete results, for all the assumed geometrical parameters and the different black hole spins.

## 3.1 Polarization degree

In Fig. 2, we show a comparison between the polarization degree for the slab, the sphere, and the cone. We plot the results for the truncated slab geometry, which is probably more consistent with the X-ray spectrum of MCG-5-23-16 (based on the reflection component, see Zoghbi et al. 2017). For the sphere, we plot the case with  $H = 30 R_G$ , which is anyway similar to the others (Fig. A3, central row). For the cone, we plot the case with  $d = 20 R_G$  (Fig. A5, center right panel). Although the inclination of the source is uncertain, a value of  $50 \pm 10$  deg is consistent with the properties of the X-ray reflection component (Weaver et al. 1998; Braito et al. 2007; Reeves et al. 2007; Guainazzi et al. 2011; Zoghbi et al. 2017). For this inclination interval, and for the case  $\Gamma = 1.8$ , the polarization degree is  $\sim 4$ –8% for the slab,  $\sim 1$ % for the sphere, and around 2–5% for the cone (Fig. 2, central row). In any case, the highest polarization degrees are obtained for the slab corona, with values up to 12%, while for a spherical corona the polarization degree is always below 3%. The conical corona produces intermediate values, in any case below 8%.

Using the same geometries as above, we plot in Fig. 3 the polarization degree as a function of the energy, in the 2–8 keV band, now divided into three energy bins. For simplicity, we plot the results only for  $\Gamma = 1.8$ ,  $kT_e = 50$  keV and for three different values of the inclination, namely 25, 50 and 75 deg, respectively. In all cases, the slab corona produces the largest polarization degrees.

## 3.2 Polarization angle

The polarization angle is also a crucial observable parameter. For the slab, it is always close to 180 deg, while it is mostly scattered around 90 deg for the spherical and conical geometries (Fig. 4). In these two latter cases, when the polarization degree is very low, the scatter in polarization angle can be quite large. This indicates a large

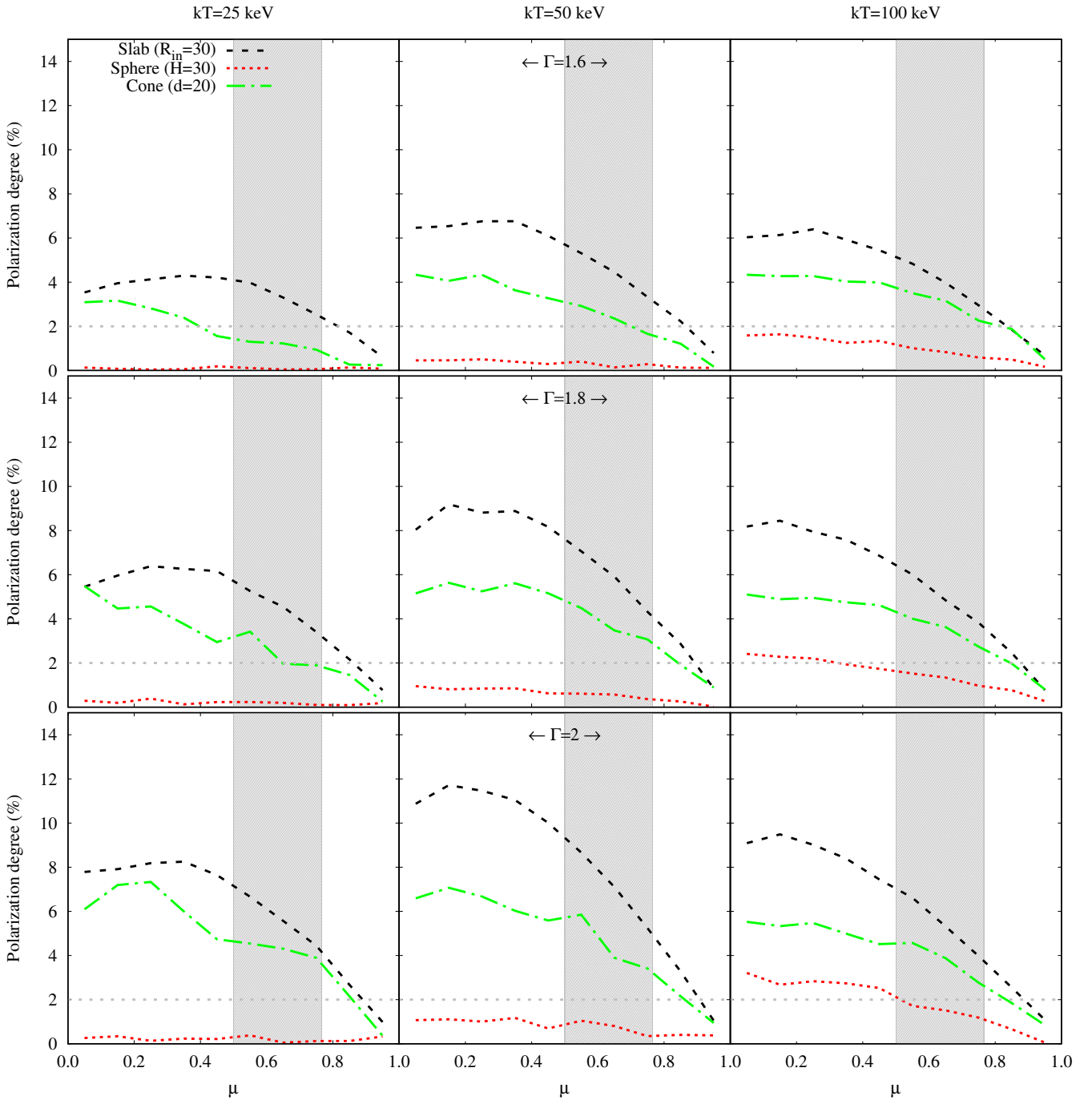


**Figure 2.** Comparison between the polarization degrees (2–8 keV) for the slab, spherical, and conical geometry, plotted versus the cosine of the inclination angle of the observer. The different rows show the results for the different X-ray photon indices assumed (from top to bottom:  $\Gamma = 1.6, 1.8,$  and  $2$ ), while the different columns correspond to the different coronal temperatures (from left to right:  $kT_c = 25, 50$  and  $100$  keV). The shaded area corresponds to the inclination interval 40–60 deg, while the gray dotted line shows the minimum polarization detectable by *IXPE* in a 500 ks exposure of MCG-5-23-16.

uncertainty in the polarization angle when the observed radiation is almost unpolarized.

In Fig. 5, we plot the polarization angle as a function of the energy, for three different geometries, like in Fig. 3. We note that the difference in polarization angle between the slab and the spherical/conical corona is not strongly dependent on the energy, nor on the inclination.

#### 4 DISCUSSION AND CONCLUSIONS

The geometrical shape of the X-ray corona of AGNs cannot be constrained via spectroscopy. Thanks to future missions like *IXPE*, X-ray polarimetry will open a new observational window, adding two observable parameters: the polarization degree and the polarization angle. We performed simulations with the relativistic Monte-Carlo

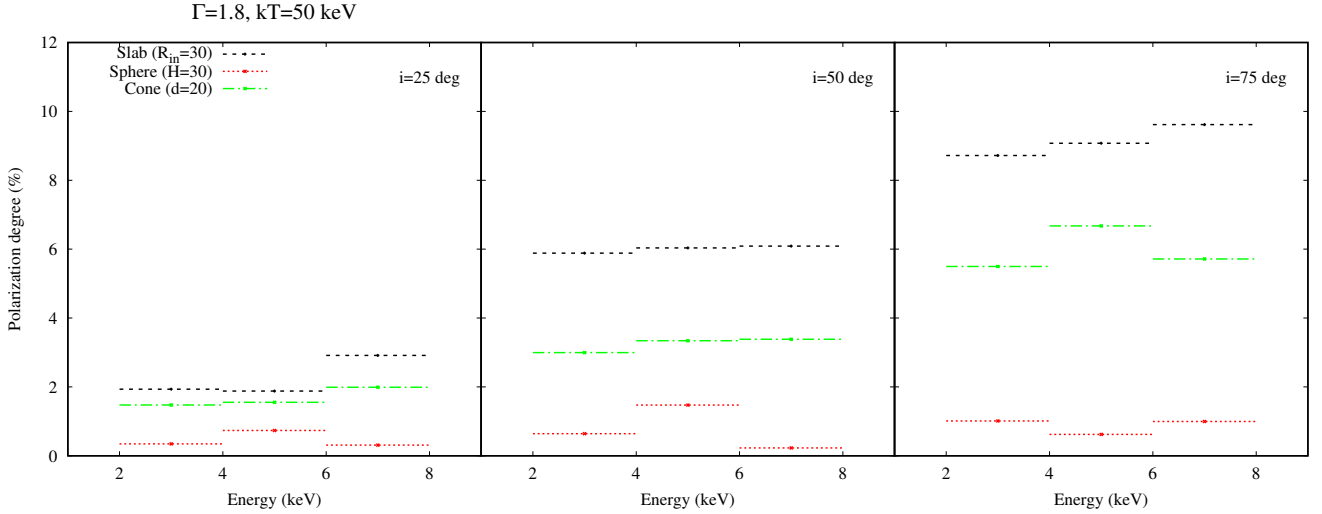


**Figure 3.** Polarization degree versus energy, for three different geometries in the case  $\Gamma = 1.8$ ,  $kT_e = 50$  keV. Each plot correspond to a different value of the inclination (from left to right: 25, 50 and 75 deg).

**Table 3.** Summary of the results (polarization degree and angle) for the three coronal geometries.

	pol. degree	pol. angle
slab	high (up to 12%)	$\sim 180$ deg
sphere	low (1–3%)	$\sim 90$ deg
cone	intermediate (up to 7%)	$\sim 90$ deg

Comptonization code `MONK`, showing that the polarimetric signal expected from AGN coronae is significantly different depending on the coronal geometry. We focused on the case of MCG-5-23-16, a very promising candidate for upcoming *IXPE* observations. Our main results are summarized in Table 3 (see also Appendix A).

A slab corona yields relatively large polarization degrees, up to 12% depending on the inclination. A spherical corona mostly yields very low polarization degrees, below 1%; we obtain values of 2–3% only for the most extended (radius of  $10 R_G$ ) and distant (height of  $30 R_G$  above the disc) case, as shown in Fig. 2. The reason could be that a more extended/distant lamppost corona is more illuminated from the bottom, meaning that the seed photon distribution is less isotropic. However, even in this case, the polarization degree is less than in the slab configuration. A conical corona, on the other hand, yields polarization degrees (for a given inclination) mostly between the slab and spherical cases. For a given set of physical parameters, the polarization degree also depends on the size of the corona (see also Beheshtipour et al. 2017; Tamborra et al. 2018) which in turn depends on the black hole spin (Dovčiak & Done 2016; Ursini et al. 2020). This is more clearly shown in the Appendix A.

According to these results, distinguishing between the different geometries is well within the capabilities of *IXPE* (see also Marinucci et al. 2019). In general, the sensitivity of a polarimeter is quantified by the minimum detectable polarization (MDP). The MDP at 99% confidence level is (e.g. Weisskopf et al. 2010):

$$\text{MDP}_{99} = \frac{4.29}{M S} \sqrt{\frac{S+B}{T}} \quad (1)$$

where  $M$  is the modulation factor,  $S$  is the source count rate,  $B$  is the background count rate and  $T$  is the observation length. For *IXPE*, the

MDP<sub>99</sub> is 2% for an observation of 500 ks of an AGN with a 2–10 keV flux of  $1 \times 10^{-10}$  erg cm<sup>-2</sup> s<sup>-1</sup> such as MCG-5-23-16 (assuming  $\Gamma = 1.8$ ). We can also estimate the uncertainty on the measurement of the polarization degree, following Kislat et al. (2015):

$$\sigma_p \approx \sqrt{\frac{2}{SM^2}}. \quad (2)$$

The same *IXPE* observation as above would yield an uncertainty of about 0.7%.

In combination with the polarization degree, the polarization angle may allow us to break the degeneracy between different geometries with high significance, if the orientation of the system is known or at least can be assumed from independent measurements. Indeed, in most cases there is a difference of 90 degrees among the slab and the spherical or conical coronae. In the latter two cases, the polarization angle is not well constrained when the polarization degree is very low. This happens especially for high values of the coronal optical depth (see also Tamborra et al. 2018). However, even in this case, the slab geometry can be ruled out.

It is important to remark that the primary X-ray emission from the corona can be reprocessed by the accretion disc or the dusty torus at larger distances. This produces a reflection component, ubiquitously observed in the X-ray spectrum of Seyferts, consisting of a fluorescence iron line and a Compton hump peaking at 20–30 keV (e.g. George & Fabian 1991; Matt et al. 1991). Theoretical models predict a degree of polarization of the reflected component as high as  $\sim 30\%$  (Matt et al. 1989; Dovčiak et al. 2004; Marin et al. 2018a). However, the actual contribution to the total polarization degree depends on the relative strength of reflection compared with the primary emission, which is expected to be low in the energy range typical of photoelectric polarimeters. Given the values measured in Compton-thin AGNs (e.g. Zappacosta et al. 2018; Panagiotou & Walter 2019), the contribution of the Compton reflection component to the total 2–8 keV flux is 5–10%. This means that the contribution to the polarization degree in this band should be no more than 3%, at least for Compton-thin AGNs (see also Marin et al. 2018b). Finally, the net observed polarization critically depends on the relative orientation of the polarization pseudovectors, meaning that the polarization de-

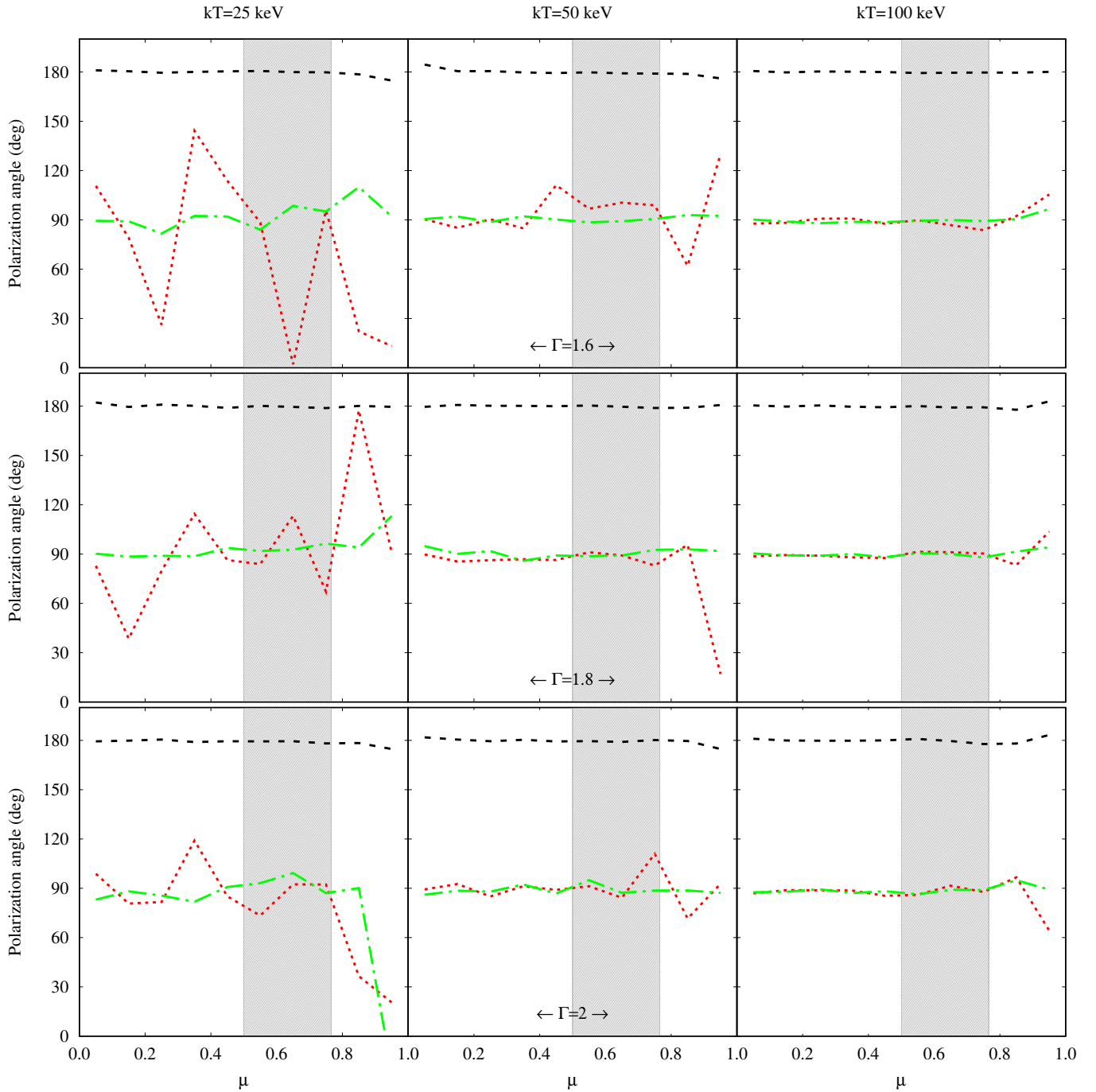


**Figure 4.** Polarization angle (in degrees) for the slab, spherical, and conical geometry, versus the cosine of the inclination angle. Line and color coding are the same as Fig. 2.

gree increases if the components are parallel and decreases if they are orthogonal. Despite these complexities, broad-band spectroscopy allows us to properly disentangle the reflection component from the primary continuum, as in the case of MCG-5-23-16 (Zoghbi et al. 2017). This will in turn allow us to assess the different contributions to the polarization spectrum with empirical fits. This approach is beyond the scope of this paper, however the simulations discussed here will be a key ingredient to robustly model the X-ray polarimetric signal of AGNs.

We note that measuring the physical parameters of the corona is of prime importance to restrict the parameter space and properly compare theoretical predictions with observations. A bright source like MCG-5-23-16, which is seen at an intermediate inclination and has a quite standard X-ray photon index, is optimal to constrain the polarization signal and, in so doing, the coronal geometry. This will in turn constrain the physical origin of the corona, which is still an open problem.

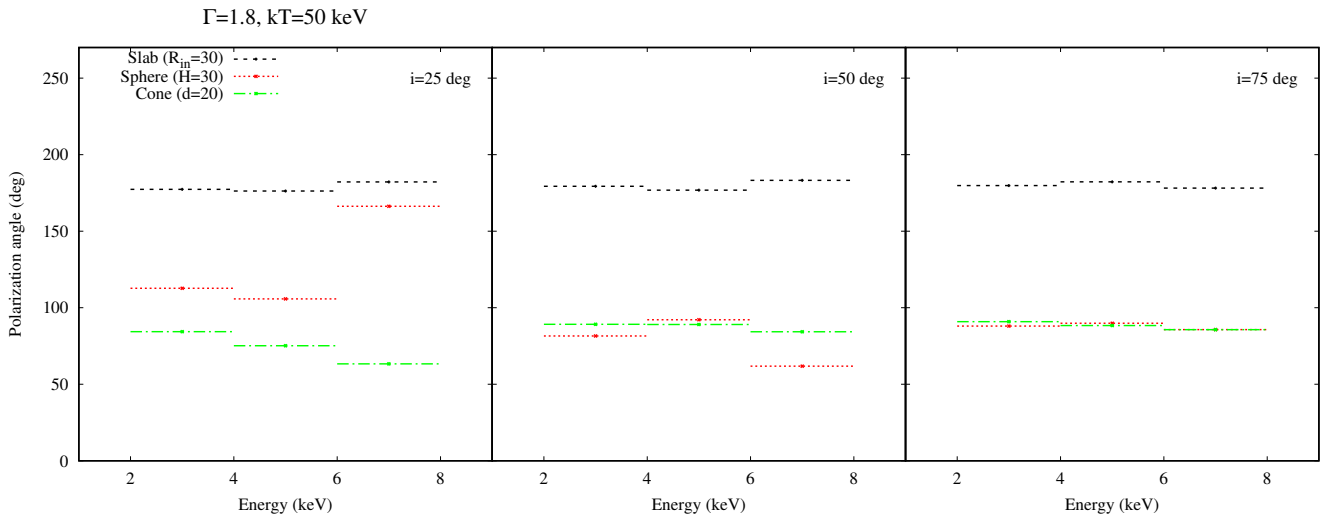


**Figure 5.** Polarization angle versus energy, for the same geometries as in Fig. 3.

## ACKNOWLEDGEMENTS

We thank the referee for useful suggestions that significantly improved the quality of the manuscript. FU, SB and GM acknowledge financial support from the Italian Space Agency (grants 2017-12-H.0 and 2017-14-H.0). WZ acknowledges the support by the Strategic Pioneer Program on Space Science, Chinese Academy of Sciences through grant XDA15052100.

## DATA AVAILABILITY

The code underlying this article, `MONK`, is proprietary. Simulation data supporting the findings of the article will be shared on reasonable request.

## REFERENCES

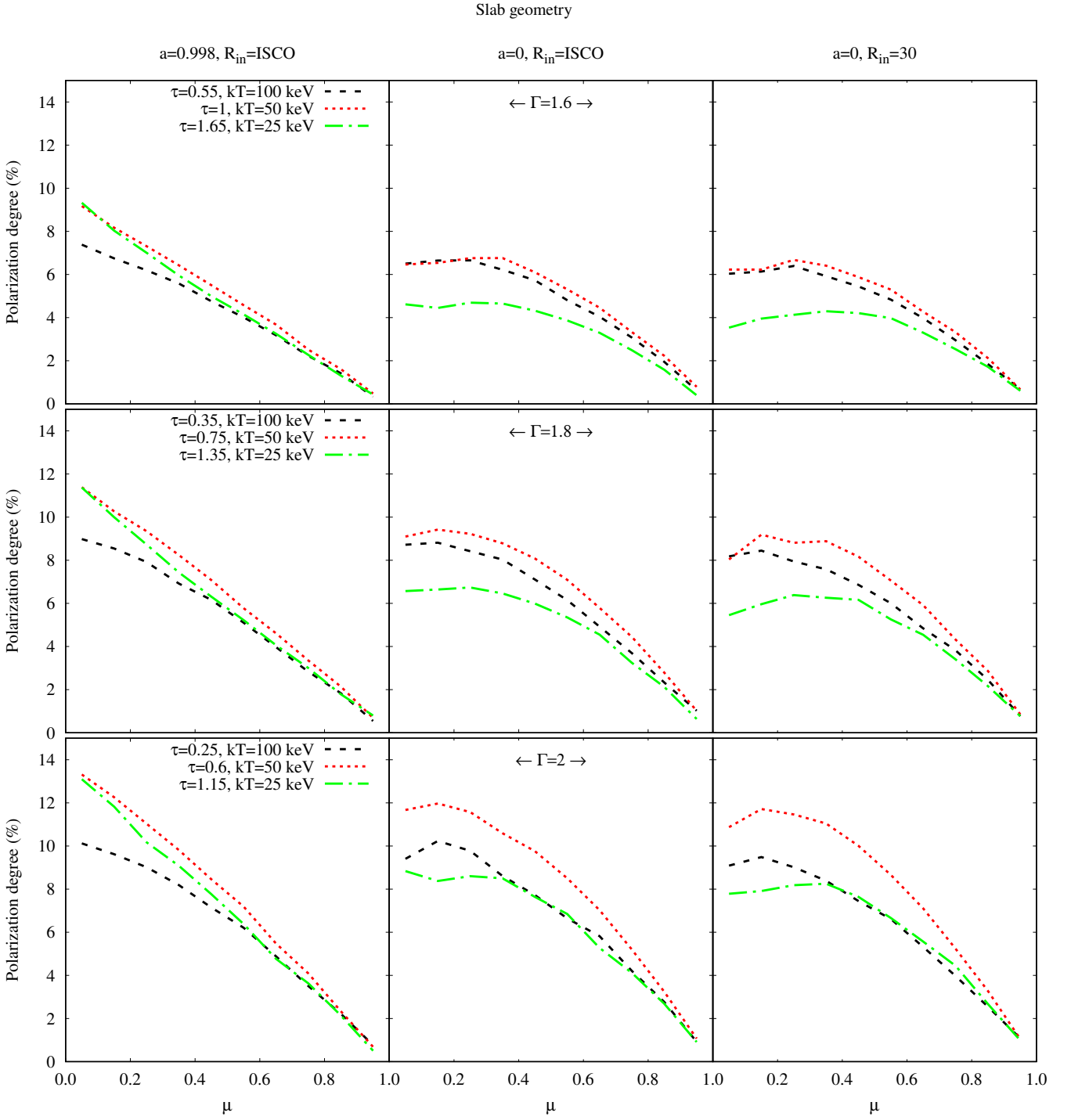
- Baloković M., et al., 2015, *ApJ*, **800**, 62
- Beheshtipour B., Krawczynski H., Malzac J., 2017, *ApJ*, **850**, 14
- Braito V., et al., 2007, *ApJ*, **670**, 978
- Caballero-García M. D., Papadakis I. E., Dovčiak M., Bursa M., Svoboda J., Karas V., 2020, *MNRAS*, **498**, 3184
- Chandrasekhar S., 1960, Radiative transfer. Dover, New York
- Chartas G., Kochanek C. S., Dai X., Poindexter S., Garmire G., 2009, *ApJ*, **693**, 174
- Chartas G., et al., 2016, *Astronomische Nachrichten*, **337**, 356
- Connors P. A., Piran T., Stark R. F., 1980, *ApJ*, **235**, 224
- Costa E., Soffitta P., Bellazzini R., Brez A., Lumb N., Spandre G., 2001, *Nature*, **411**, 662
- De Marco B., Ponti G., Cappi M., Dadina M., Uttley P., Cackett E. M., Fabian A. C., Miniutti G., 2013, *MNRAS*, **431**, 2441
- Di Matteo T., 1998, *MNRAS*, **299**, L15
- Dovčiak M., Done C., 2016, *Astronomische Nachrichten*, **337**, 441
- Dovčiak M., Muleri F., Goosmann R. W., Karas V., Matt G., 2011, *ApJ*, **731**, 75
- Dovčiak M., Karas V., Matt G., 2004, *MNRAS*, **355**, 1005
- George I. M., Fabian A. C., 1991, *MNRAS*, **249**, 352
- Ghisellini G., Haardt F., Matt G., 2004, *A&A*, **413**, 535
- Guainazzi M., Bianchi S., de La Calle Pérez I., Dovčiak M., Longinotti A. L., 2011, *A&A*, **531**, A131
- Haardt F., Maraschi L., 1991, *ApJ*, **380**, L51
- Haardt F., Maraschi L., 1993, *ApJ*, **413**, 507
- Haardt F., Matt G., 1993, *MNRAS*, **261**, 346
- Henri G., Pelletier G., 1991, *ApJ*, **383**, L7
- Henri G., Petrucci P. O., 1997, *A&A*, **326**, 87
- Kara E., Alston W. N., Fabian A. C., Cackett E. M., Uttley P., Reynolds C. S., Zoghbi A., 2016, *MNRAS*, **462**, 511
- Kislat F., Clark B., Beilicke M., Krawczynski H., 2015, *Astroparticle Physics*, **68**, 45
- Marin F., Weisskopf M. C., 2017, in Reylé C., Di Matteo P., Herpin F., Lagadec E., Lançon A., Meliani Z., Royer F., eds, SF2A-2017: Proceedings of the Annual meeting of the French Society of Astronomy and Astrophysics. p. Di ([arXiv:1708.02022](https://arxiv.org/abs/1708.02022))
- Marin F., Dovčiak M., Muleri F., Kislat F. F., Krawczynski H. S., 2018a, *MNRAS*, **473**, 1286
- Marin F., Dovčiak M., Kammoun E. S., 2018b, *MNRAS*, **478**, 950
- Marinucci A., et al., 2019, *A&A*, **623**, A12
- Markoff S., Nowak M. A., Wilms J., 2005, *ApJ*, **635**, 1203
- Matt G., Perola G. C., Costa E., Piro L., 1989, in Hunt J., Battrick B., eds, ESA Special Publication Vol. 296, Two Topics in X-Ray Astronomy, Volume 1: X Ray Binaries. Volume 2: AGN and the X Ray Background. pp 991–993
- Matt G., Perola G. C., Piro L., 1991, *A&A*, **247**, 25
- Matt G., Fabian A. C., Ross R. R., 1993, *MNRAS*, **264**, 839
- Misner C. W., Thorne K. S., Wheeler J. A., 1973, *Gravitation*
- Novikov I. D., Thorne K. S., 1973, in Dewitt C., Dewitt B. S., eds, Black Holes (Les Astres Occlus). pp 343–450
- Onori F., et al., 2017a, *MNRAS*, **464**, 1783
- Onori F., et al., 2017b, *MNRAS*, **468**, L97
- Panagiotou C., Walter R., 2019, *A&A*, **626**, A40
- Ponti G., Papadakis I., Bianchi S., Guainazzi M., Matt G., Uttley P., Bonilla N. F., 2012, *A&A*, **542**, A83
- Poutanen J., Svensson R., 1996, *ApJ*, **470**, 249
- Poutanen J., Vilhu O., 1993, *A&A*, **275**, 337
- Reeves J. N., et al., 2007, *PASJ*, **59**, 301
- Reis R. C., Miller J. M., 2013, *ApJ*, **769**, L7
- Schnittman J. D., Krolik J. H., 2010, *ApJ*, **712**, 908
- Tamborra F., Matt G., Bianchi S., Dovčiak M., 2018, *A&A*, **619**, A105
- Titarchuk L., 1994, *ApJ*, **434**, 570
- Ursini F., Dovčiak M., Zhang W., Matt G., Petrucci P. O., Done C., 2020, *A&A*, **644**, A132
- Véron-Cetty M.-P., Véron P., 2010, *A&A*, **518**, A10

- Veron P., Lindblad P. O., Zuiderwijk E. J., Veron M. P., Adam G., 1980, *A&A*, **87**, 245
- Weaver K. A., Krolik J. H., Pier E. A., 1998, *ApJ*, **498**, 213
- Weisskopf M. C., Elsner R. F., O’Dell S. L., 2010, in Arnaud M., Murray S. S., Takahashi T., eds, Society of Photo-Optical Instrumentation Engineers (SPIE) Conference Series Vol. 7732, Space Telescopes and Instrumentation 2010: Ultraviolet to Gamma Ray. p. 77320E ([arXiv:1006.3711](#)), [doi:10.1117/12.857357](#)
- Weisskopf M. C., et al., 2016, The Imaging X-ray Polarimetry Explorer (IXPE). p. 990517, [doi:10.1117/12.2235240](#)
- Wilkins D. R., Fabian A. C., 2012, *MNRAS*, **424**, 1284
- Zappacosta L., et al., 2018, *ApJ*, **854**, 33
- Zhang S. N., et al., 2016, in den Herder J.-W. A., Takahashi T., Bautz M., eds, Society of Photo-Optical Instrumentation Engineers (SPIE) Conference Series Vol. 9905, Space Telescopes and Instrumentation 2016: Ultraviolet to Gamma Ray. p. 99051Q ([arXiv:1607.08823](#)), [doi:10.1117/12.2232034](#)
- Zhang W., Dovčiak M., Bursa M., 2019, *ApJ*, **875**, 148
- Zoghbi A., et al., 2017, *ApJ*, **836**, 2

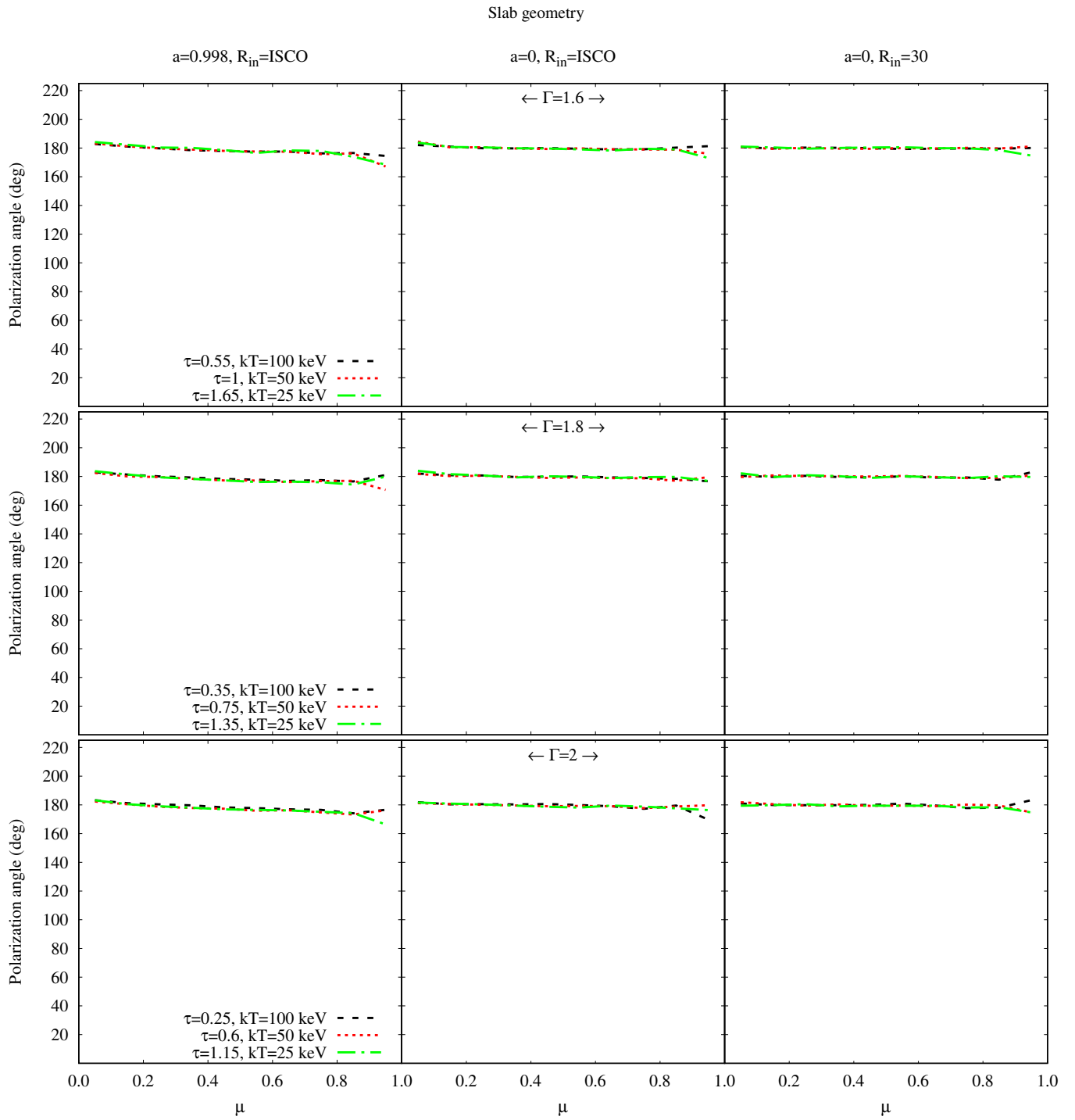
## APPENDIX A: COMPLETE RESULTS

In Figs. A1, A2, A3, A4, A5, and A6, we plot the polarization degree and angle, as a function of the inclination, for the three geometries considered in this work and for the different coronal parameters. We separate the three geometries to avoid overcrowding the plots. In these figures, different columns correspond to different coronal sizes. Interestingly, the different sizes yield different polarization degrees, as shown by Fig. A1 for the slab, Fig. A3 for the sphere, and Fig. A5 for the cone. Concerning the polarization angle, Fig. A4 shows some scatter around 90 deg in the spherical case. As argued in Sect. 3.2, this is not surprising given the low polarization degree. In the conical case, the polarization angle sometimes flips from 90 to 180 deg, especially when the optical depth is large and for observers at low inclinations (see Fig. A6). This could be due to the increasing contribution by multiply scattered photons (e.g. Tamborra et al. 2018), combined with the decreasing horizontal polarization of the disc photons for observers at low inclinations (e.g. Schnittman & Krolik 2010).

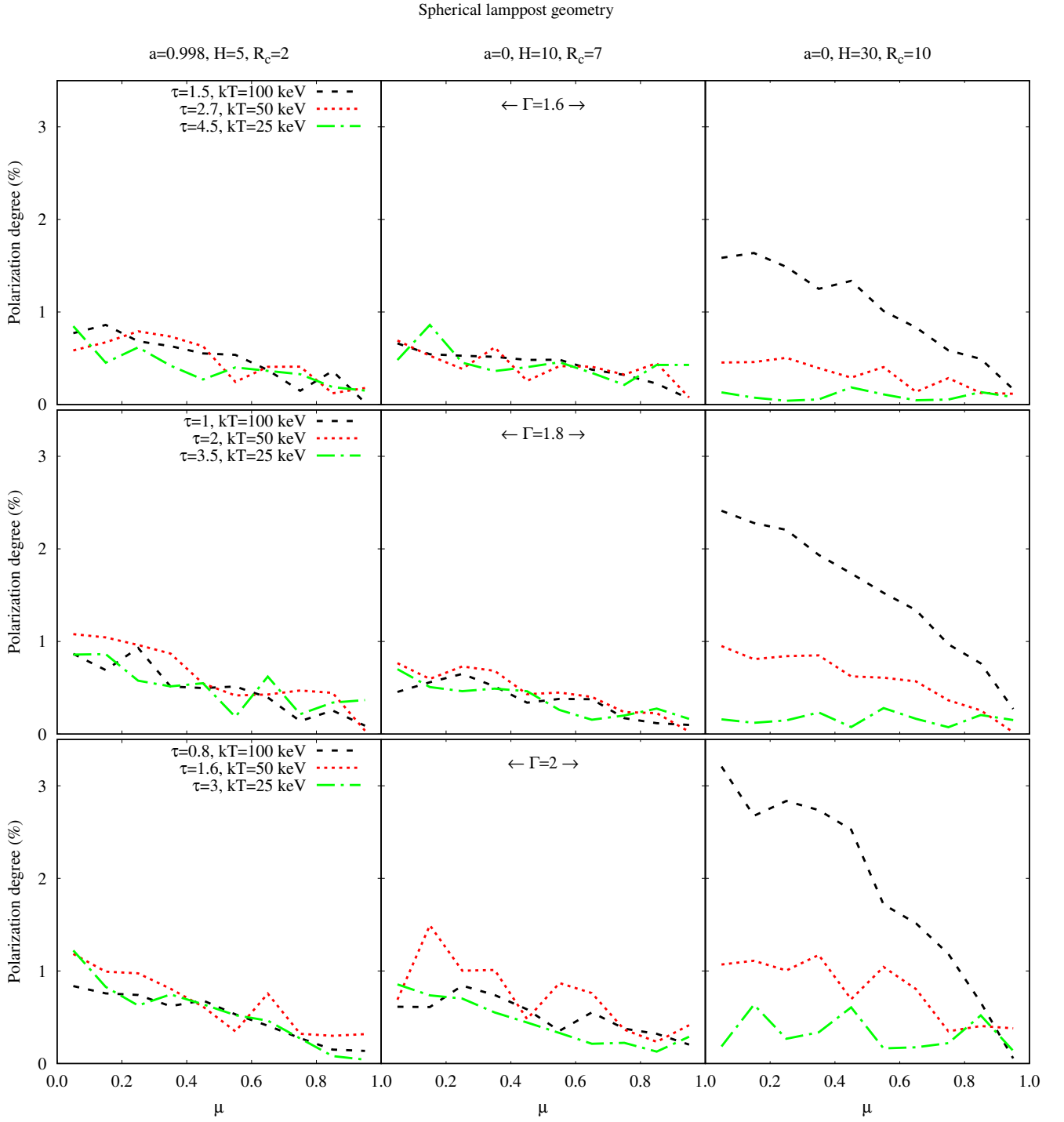
This paper has been typeset from a  $\text{\TeX}/\text{\LaTeX}$  file prepared by the author.



**Figure A1.** Polarization degree in the 2–8 keV band versus the cosine of the inclination angle of the observer, for the slab geometry. The different rows show the results for the different photon indices assumed (from top to bottom:  $\Gamma = 1.6, 1.8,$  and  $2$ ); colors and dash types highlight the different pairs  $\tau, kT_c$  reproducing the photon index (see also Table 2). Column-wise, the plot shows the results for the different black hole spin and/or inner radius of the slab (see also Table 1).

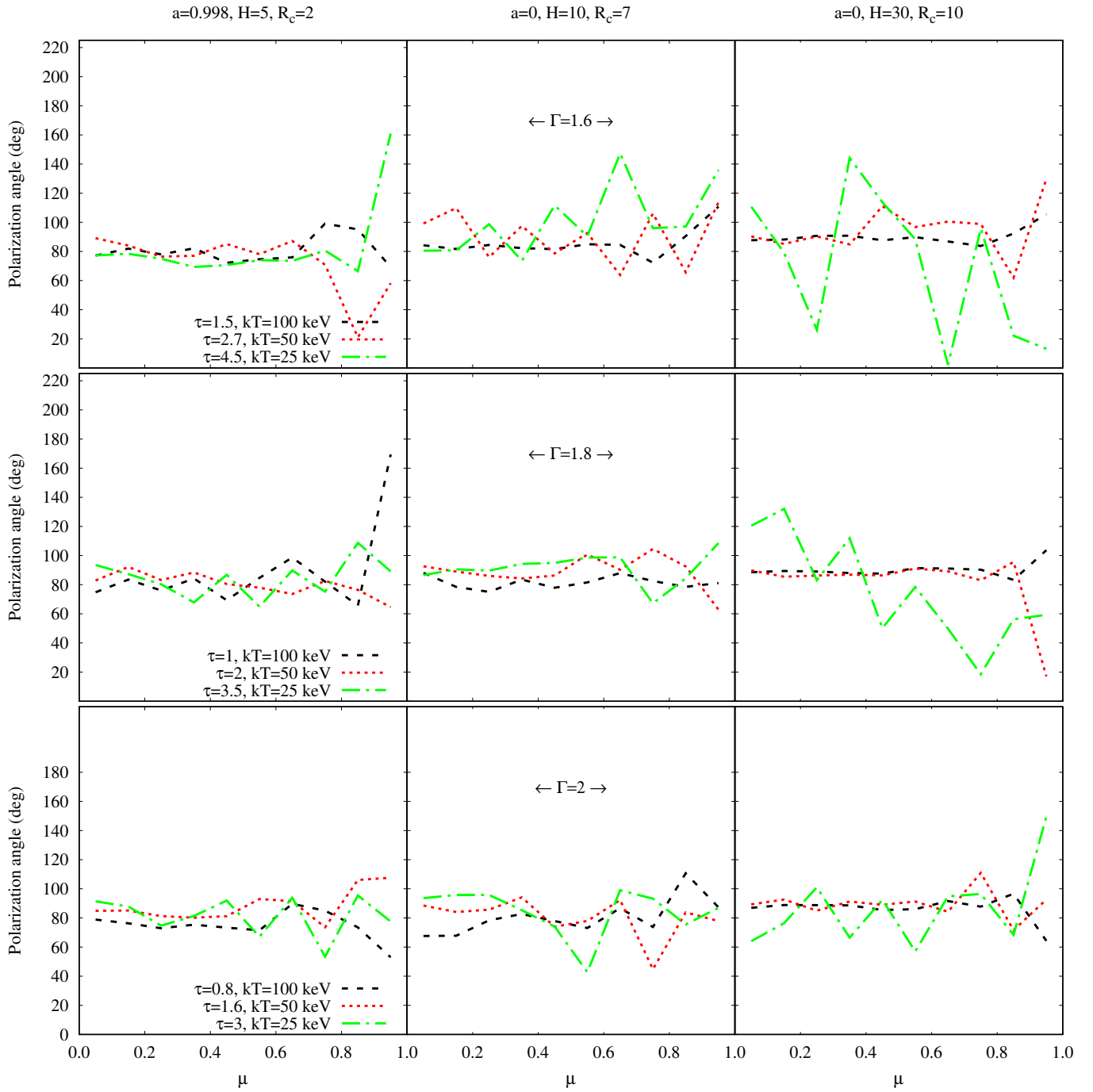


**Figure A2.** Polarization angle versus the cosine of the inclination angle, for the slab geometry.



**Figure A3.** Polarization degree versus the cosine of the inclination angle, for the spherical geometry. Different columns correspond to different values of the height and radius of the corona. Note the different y-axis scale compared with Fig. A1.

## Spherical lamppost geometry

**Figure A4.** Polarization angle versus the cosine of the inclination angle, for the spherical geometry.

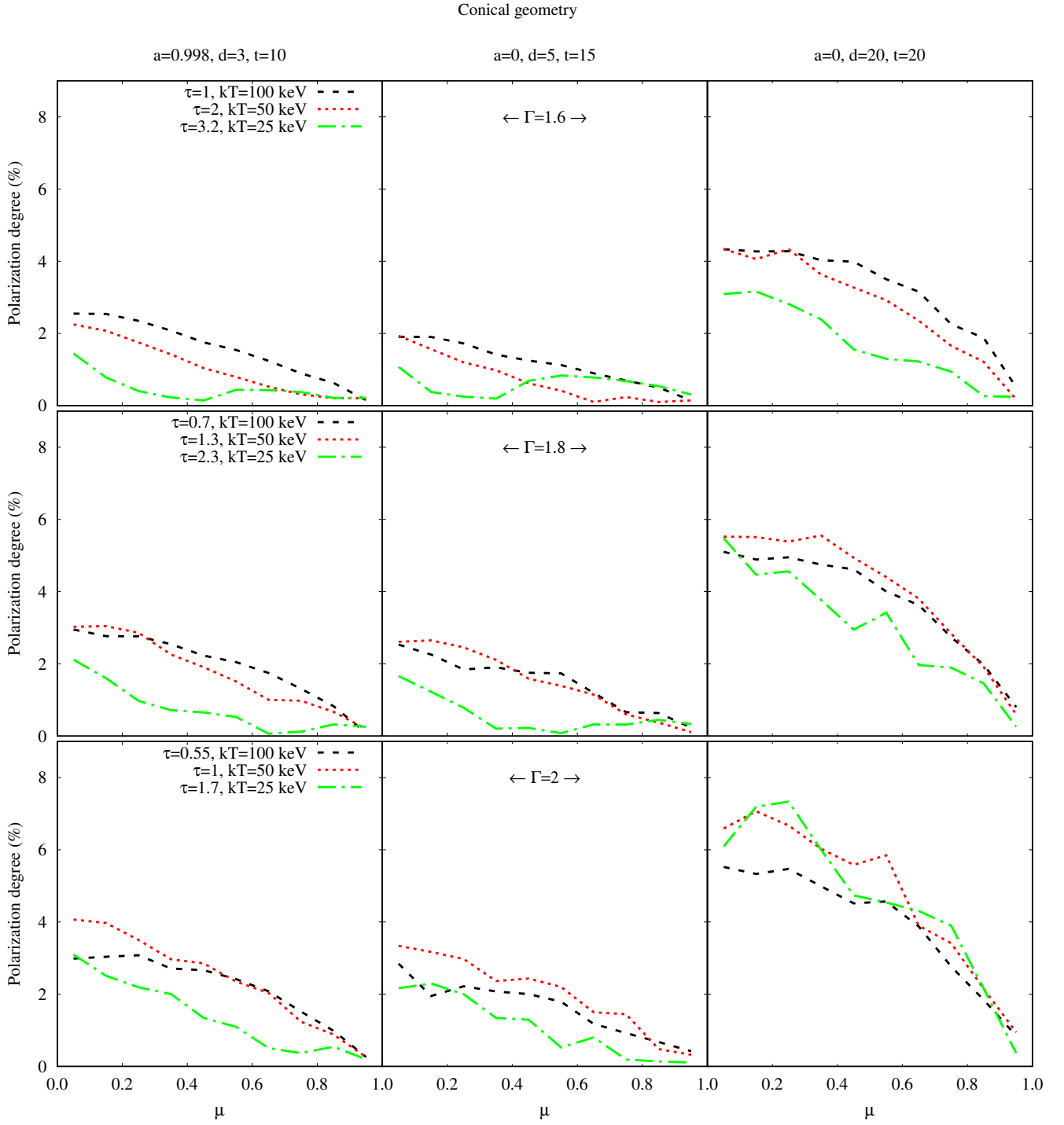


**Figure A5.** Polarization degree versus the cosine of the inclination angle, for the conical geometry.

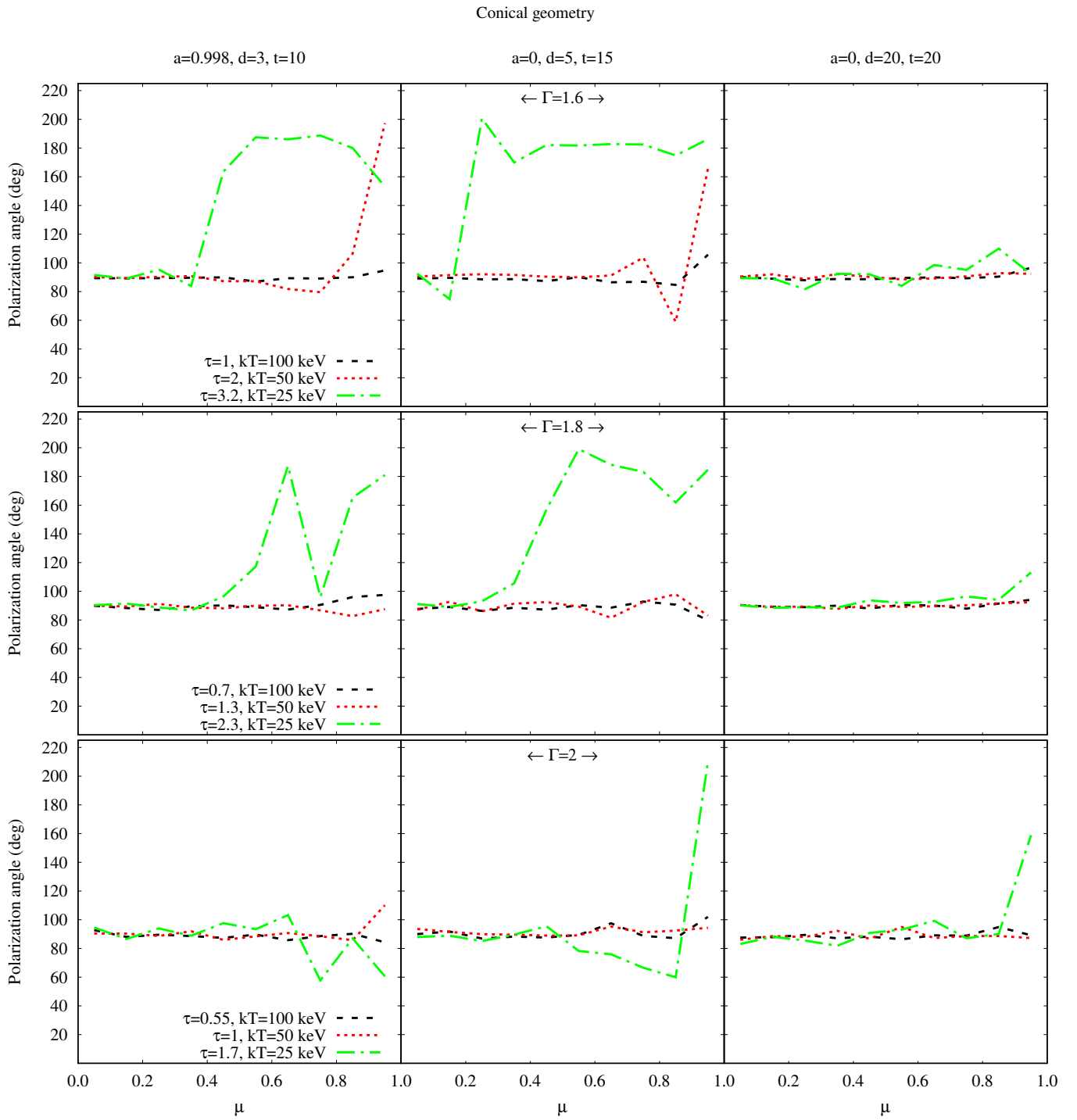


**Figure A6.** Polarization angle versus the cosine of the inclination angle, for the conical geometry.